

# Multi-Space-Object Tracking with the Poisson Labeled Multi-Bernoulli (PLMB) Filter & Probabilistic Admissible Region Constraints

**Leonardo Cament**  
**Martin Adams**

**Pablo Barrios**

*Department of Electrical Engineering & Advanced Mining Technology Center (AMTC),  
Universidad de Chile, Santiago 8370451, Chile.*

## ABSTRACT

The number of space objects (SOs) in orbit has increased dramatically in recent years making methodologies to improve track catalogs crucial. Therefore, the Poisson Labelled Multi-Bernoulli (PLMB) multi-target tracking filter, based on the recent Random Finite Set (RFS) framework, is proposed. It adopts labeled multi-Bernoulli target and Poisson birth distributions, which, in contrast with other recent RFS approaches, makes it compatible with useful partially uniform SO birth and probabilistic admissible region initial orbit determination methods. In contrast to our prior work, kinematic modelling using a Lie based target state representation is used to preserve the geometric characteristics of true SO uncertainty, permitting high motion prediction accuracy over extended periods during which no observations occur.

**Keywords**— Multi-target tracking, Space situational awareness, Random Finite Sets, Poisson Labeled Multi-Bernoulli (PLMB) filter, Lie group, Riemannian manifolds.

## 1. INTRODUCTION

The efficient detection, tracking, and cataloging of orbiting space objects (SOs) are of paramount importance for improved Space Situational Awareness (SSA) and the demand for modern SO tracking applications to produce more accurate and more computationally efficient tracking capabilities is higher than ever.

Due to the random nature of various forces which act on SOs, their orbits can change significantly over time. Therefore, stochastic estimation methods have been popular for updating the track catalogs of SOs [1, 2, 3]. Recent approaches model the multi-target state of SOs with a probability density function. Such approaches usually initialize the tracks of observed SOs using Initial Orbit Determination (IOD), where an initial estimate of the orbit is refined with observations using a non-linear optimization approach. The estimated states of the SOs are propagated via a recursive Bayesian filter based on subsequent observations. Bayesian approaches have been based on Multiple Hypothesis Tracking (MHT) [4, 5] and more recently Random Finite Set (RFS) [6, 7] concepts, which jointly estimate target number as well as their state values.

To improve the important IOD component in SO tracking, recent work has advocated the use of a Probabilistic Admissible Region (PAR) [8], which is an orbital Admissible Region (AR) [1] for SOs that, combined with a partially uniform birth (PUB) [9] concept, adheres to the assumption of independence between newborn and surviving targets. Recent notable articles which have combined the use of Bayesian RFS tracking methods with the PAR, IOD approach in SSA, include those by B. Jones et al. in which an RFS based Cardinalized Probability Hypothesis Density (CPHD) filter is adopted. Recent RFS multi-target tracking (MTT) approaches have focused on labeled filters such as the Labeled Multi-Bernoulli (LMB) [10] and the Poisson Labeled Multi-Bernoulli (PLMB) [11] filters, which jointly estimates the state and unique identities for each target track.

In [12] a PUB-PAR-PLMB filter was developed. It consists of a labeled multi-Bernoulli distribution propagated in time and a Poisson distribution that models SO births. The PLMB filter is capable of tracking and identifying targets with unique labels, and has been shown to out-perform the CPHD filter in a manner similar to the LMB filter. In contrast to

other labeled RFS approaches however, it accommodates the PAR-PUB SO birth concept, allowing this powerful IOD method to be incorporated into the filtering framework. The PUB density generates uniformly distributed potential SO births in the sensor field of view (FoV) along with a Gaussian Mixture (GM) of the semi-major axis length and eccentricity, constrained by physical energy considerations. The PAR approach allows the calculation of a particle distribution during the update which obeys the orbital energy constraints. This corresponds to a maximum value of the semi-major axis length and eccentricity values representing Low Earth Orbit (LEO) SOs.

The spatial SO state is usually modelled by a 3D position and velocity GM in the Earth-Centered Inertial frame. It is however known that the orbital kinematic process evolves according to a “banana shaped” distribution, and that the GM fails to accurately predict SO states. Published solutions to this problem include splitting each component of the GM into several Gaussian components; however this substantially increases the computational complexity. Other solutions use a particle distribution [12], requiring many particles, the states of which are directly predicted by the kinematic model. However, since the kinematic model is complex the use of particles can be computationally expensive since the non-linear SO kinematic model not only includes the Earth’s central body gravity, but also other forces, including gravity due to the sun and moon, the non-spherical gravitational potential of the Earth, atmospheric drag and solar radiation pressure. Therefore in this article, the Lie Special Euclidean group  $SE(3) \times \mathbb{R}^3$  will be used to model the SO state and kinematics, since such models preserve the geometric characteristics of SO motion, permitting higher accuracy for extended periods of time, without increase of computational complexity. The former is particularly important due to the often low observational times of SOs. In particular an Unscented Kalman Filter (UKF) [13, 14] implementation of the SO Lie based prediction is developed for each single target component within the multi-target PLMB filter.

Experiments are demonstrated using simulated SO trajectories created from real Two-Line Element (TLE) data, with simulated measurements from twelve telescopic observatories, which form part of the Falcon Telescope Network (FTN) [15]. A comparison between the proposed PLMB filter based on SO Lie group state models with a standard Monte Carlo particle distribution used for state prediction together with a linear GM model during the measurement update is given.

The article will demonstrate that the combination of the PLMB filter and PAR, IOD process provides promising target tracking capabilities for multiple SOs, particularly under short time observation periods. An improvement in computational efficiency will also be demonstrated based on the Lie  $SE(3) \times \mathbb{R}^3$  group modelling and UKF single target estimation component, due to a vast reduction in the necessary number of particles (Sigma Points within the UKF) when compared with the Monte Carlo (MC) prediction strategy used in [12].

## 2. TARGET STATE REPRESENTATION

Usually, a target’s state is represented by a Gaussian or GM distribution. These distributions have the advantage of being easy to propagate using the Kalman filter. However for SO tracking a Gaussian distribution is often a poor approximation due to the non-linear nature of the SO kinematics. Another possibility is to model the state as weighted particles, for which kinematic propagation is relatively simple to implement, but computationally expensive due to the large number of particles required. Here, we therefore propose the use of a state in the Lie group  $SE(3) \times \mathbb{R}^3$ , which follows a distribution referred to as a Concentrated Gaussian Distribution (CGD). This has the advantage that one of the degrees of freedom of the distribution is constraint to a sphere and is a better fit to the “banana shape” of the real SO distributions in LEO.

### 2.1 Target State

The proposed state is expressed as the following CGD:

$$p(\boldsymbol{\chi}) = \text{Exp}(\boldsymbol{\xi})\bar{\boldsymbol{\chi}}, \boldsymbol{\xi} \sim \mathcal{N}(\mathbf{0}, \mathbf{P}) \quad (1)$$

where  $\boldsymbol{\chi}$  is the state,  $\bar{\boldsymbol{\chi}}$  and  $\mathbf{P}$  are the mean and the covariance matrices of the CGD distribution respectively, and  $\boldsymbol{\xi}$  represents a random sample from the Normal distribution, which is projected into the  $SE(3) \times \mathbb{R}^3$  space by the exponential function. As can be seen, the mean  $\bar{\boldsymbol{\chi}} \in SE(3) \times \mathbb{R}^3$ , however  $\boldsymbol{\xi} \in \mathbb{R}^9$  is in the tangent space surrounding the mean. Note that the CGD is not a Gaussian distribution and therefore, the Kalman filter is not directly applicable.

The target state in Cartesian coordinates is composed of position and velocity  $\mathbf{x} = [\mathbf{p}^T, \mathbf{v}^T]^T$ . The mean  $\bar{\boldsymbol{\chi}}$  can be

represented by the  $8 \times 8$  matrix:

$$\bar{\boldsymbol{\chi}} = \begin{bmatrix} \mathbf{I}_3 & \bar{\mathbf{p}} \\ \mathbf{0} & 1 \\ & & \mathbf{I}_3 & \bar{\mathbf{v}} \\ & & \mathbf{0} & 1 \end{bmatrix} \quad (2)$$

where the spaces are filled with the appropriate number of zeros and  $\mathbf{I}_3$  is the identity matrix of dimensions 3.

The random vector  $\boldsymbol{\xi} = [\boldsymbol{\rho}^T, \boldsymbol{\theta}^T, \mathbf{v}^T]^T$ , where  $\boldsymbol{\rho}$  and  $\boldsymbol{\theta}$  represent components of a vector in the tangent space of  $SE(3)$ . Note that the covariance matrix  $\mathbf{P}$  is of dimension  $9 \times 9$ . In this manner the state can be represented with the parameters  $\{\bar{\boldsymbol{\chi}}, \mathbf{P}\}$  or equivalently  $\{\bar{\mathbf{x}}, \mathbf{P}\}$ .

## 2.2 Conversion of the Weighted Particle into a Concentrated Gaussian Distribution

Since in this work the UKF and PAR methods are used, and both methods result in a weighted particle distribution, we propose a methodology for conversion to a CGD. The weighted particle distribution  $\{\gamma^j, \mathbf{x}^j\}_1^J$  is converted into a CGD represented by a mean state  $\bar{\boldsymbol{\chi}}$  in the Lie Group  $SE(3) \times \mathbb{R}^3$  and a covariance matrix in the surrounding tangent space. Firstly, the position components of the particles  $\mathbf{p}^j$  are normalized as unit vectors  $\mathbf{p}_u^j = \mathbf{p}^j / \|\mathbf{p}^j\|$ . We use the algorithm in [16] to obtain the weighted average of  $\{\gamma^j, \mathbf{p}_u^j\}_1^J$  in  $S^2$  (the unit sphere). It is calculated using the Gauss–Newton iterative algorithm by initiating  $\bar{\mathbf{p}}_u$  as the simple average of  $\{\gamma^j, \mathbf{p}_u^j\}_1^J$ , normalized to be a unit vector. Then the following equation is iterated until a tolerable error between two consecutive values is obtained.

$$\bar{\mathbf{p}}_u \leftarrow \text{Exp}_{S^2} \bar{\mathbf{p}}_u \left( \sum_{j=1}^J \gamma^j \text{Log}_{S^2} \bar{\mathbf{p}}_u (\mathbf{p}_u^j) \right), \quad (3)$$

where logarithmic, exponential maps are defined in the Appendix A as well as other functions and operators, such as, *hat* ( $\wedge$ ) and *vee* ( $\vee$ ).

The rotation matrix  $\mathbf{R}^j$ , such that  $\mathbf{p}_u^j = \mathbf{R}^j \bar{\mathbf{p}}_u$ , is obtained as:

$$\begin{aligned} \mathbf{w} &= \bar{\mathbf{p}}_u \times \mathbf{p}_u \\ \cos \theta &= \bar{\mathbf{p}}_u^T \cdot \mathbf{p}_u \\ \mathbf{R} &= \mathbf{I} + \mathbf{w}^\wedge + \frac{\mathbf{w}^\wedge^2}{1 + \cos \theta}. \end{aligned} \quad (4)$$

Then,  $\bar{\mathbf{p}} = \sum_{j=1}^J \gamma^j \mathbf{R}^j \mathbf{p}^j$ . Each  $\mathbf{p}^j = \mathbf{R}^j \bar{\mathbf{p}} + \mathbf{t}^j$ , thus  $\mathbf{t}^j = \mathbf{R}^j \bar{\mathbf{p}} - \mathbf{p}^j$ .

Equivalently  $[\mathbf{p}^{jT} \ 1]^T = \mathbf{M}^j [\bar{\mathbf{p}}^T \ 1]^T$ , where  $\mathbf{M}^j$  is the homogeneous matrix as a member of the Lie group  $SE(3)$ , is given by:

$$\mathbf{M}^j = \begin{bmatrix} \mathbf{R}^j & \mathbf{t}^j \\ \mathbf{0} & 1 \end{bmatrix} \quad (5)$$

The weighted average velocity is  $\bar{\mathbf{v}} = \sum_{j=1}^J \gamma^j \mathbf{v}^j$ . Define a new matrix  $\mathbf{A} = \text{diag}(\mathbf{M}^j, \mathbf{B}^j)$ , with:

$$\mathbf{B}^j = \begin{bmatrix} \mathbf{I} & \mathbf{v}^j - \bar{\mathbf{v}} \\ \mathbf{0} & 1 \end{bmatrix} \quad (6)$$

The covariance matrix is then:

$$\mathbf{P} = \sum_{j=1}^J \gamma^j \text{Log}(\mathbf{A}^j) \text{Log}(\mathbf{A}^j)^T. \quad (7)$$

The procedure explained in this Subsection is referred to as the function  $\{\bar{\boldsymbol{\chi}}, \mathbf{P}\} = \text{PARTICLES TO CGD}(\{\gamma^j, \mathbf{x}^j\}_1^J)$ .

### 3. MULTI SO INITIALIZATION

Multi-SO initialization is composed of two components, namely the use of a PUB during the prediction step, and the PAR approach, which provides the single SO spatial density parameters in the update step.

Inspired by the PUB-CPHD filter in [9], a PUB-PLMB filter, combined with the PAR method for modeling the initial state of a telescopic based measurement, is adopted. The PAR is an AR which adheres to the assumption of independence between newborn and surviving targets [9]. In contrast to the PUB-CPHD filter, the proposed PUB-PLMB filter is a true multi-target tracking filter in that it estimates the identification of each target at each time step in the form of a unique label. Furthermore, recent articles such as [11, 17, 18] have demonstrated superior multi-target tracking performance with labeled filters such as the PLMB filter, as opposed to non-labeled approaches such as the Probability Hypothesis Density (PHD) and CPHD filters.

#### 3.1 Partially Uniform Birth (PUB) Multi-Target Initiation Model

The PUB intensity generates a uniformly distributed birth density in the sensor FoV, with intensity function given by:

$$D_{\mathcal{B}}(\mathbf{x}) = \lambda_{\beta} \cdot \mathcal{U}(\boldsymbol{\theta}(\mathbf{x}); \mathcal{B}) \cdot \sum_{i=1}^{J_B} w_b^{(i)} \mathcal{N}(\boldsymbol{\phi}(\mathbf{x}); \bar{\boldsymbol{\phi}}^{(i)}, \mathbf{P}_{\phi}^{(i)}), \quad (8)$$

where  $\mathbf{x}$  is a target state in the Earth-Centered Inertial (ECI) frame,  $\boldsymbol{\theta}(\mathbf{x})$  is a function that maps the target state to the observable part of the state, which, for a telescopic image, is given by  $\boldsymbol{\theta}(\mathbf{x}) = [\alpha, \beta, \dot{\alpha}, \dot{\beta}]^T$ . In this case,  $\boldsymbol{\phi}(\mathbf{x}) = [s, \dot{s}]^T$  is the non-observable part of the state, where  $s$  is the distance between the observer and the target and  $\dot{s}$  is the radial velocity of the target. Note that the joint vector  $[\boldsymbol{\theta}(\mathbf{x})^T, \boldsymbol{\phi}(\mathbf{x})^T]^T$  is the target state in the telescopic camera coordinate system.  $\lambda_{\beta}$  is the expected number of targets of the Poisson intensity,  $\mathcal{U}(\boldsymbol{\theta}(\mathbf{x}); \mathcal{B})$  represents the uniform density for the observable part of the target state with boundary  $\mathcal{B}$  given by the sensor FoV. The non-observable part of the state is modeled by a GM density of  $J_B$  components  $\mathcal{N}(\boldsymbol{\phi}(\mathbf{x}); \bar{\boldsymbol{\phi}}^{(i)}, \mathbf{P}_{\phi}^{(i)})$ , each with weight  $w_b^{(i)}$ , mean vector  $\bar{\boldsymbol{\phi}}^{(i)}$  and covariance matrix  $\mathbf{P}_{\phi}^{(i)}$ .

#### 3.2 Probabilistic Admissible Region (PAR) Approach for New Target Density Approximation

The PAR approach is an orbital admissible region that adheres to the assumption of independence between newborn targets and surviving SOs. These SOs obey physical energy constraints in terms of orbital semi-major axis length and eccentricity within a range of orbits of interest. In this article, LEO SOs are considered.

The new SO distribution is modeled by the multiplication of the birth intensity  $D_{\mathcal{B}}(\mathbf{x})$  and the measurement likelihood distribution  $l_z(\mathbf{z}|\mathbf{x})$ , which will be shown in detail in Section 4:

$$D_{\mathcal{B}}(\mathbf{x})l_z(\mathbf{z}|\mathbf{x}) \approx \lambda_{\beta} \cdot \mathcal{N}(\boldsymbol{\theta}(\mathbf{x}); \mathbf{z}, \mathbf{R}) \cdot \sum_{i=1}^{J_B} w_b^{(i)} \mathcal{N}(\boldsymbol{\phi}(\mathbf{x}); \bar{\boldsymbol{\phi}}^{(i)}, \mathbf{P}_{\phi}^{(i)}), \quad (9)$$

where  $\mathcal{N}(\boldsymbol{\theta}(\mathbf{x}); \mathbf{z}, \mathbf{R})$  is a Gaussian distribution on  $\boldsymbol{\theta}(\mathbf{x})$  modelling the resulting observable density for a given measurement  $\mathbf{z}$ , with sensor noise matrix  $\mathbf{R}$  ([9], pp. 1459).

In order to estimate the non-observable part of the state  $\boldsymbol{\phi}(\mathbf{x}) = [s, \dot{s}]^T$  based on constraints provided by the measurements, the PAR [2, 19, 9] methodology is used. More details about the Constrained Admissible Region (CAR)/PAR methods, including equations and their parameters, are given in [12, appendix A]. The constraint regions are, for constraint 1:

$$c_1(\boldsymbol{\theta}, \boldsymbol{\phi}; \mathbf{q}) = s^2 + w_1 \dot{s} + F(s) + \frac{\mu}{a} = 0 \quad (10)$$

and for constraint 2:

$$c_2(\boldsymbol{\theta}, \boldsymbol{\phi}; \mathbf{q}) = \gamma_4 s^4 + \gamma_3 s^3 + \gamma_2 s^2 + \gamma_1 \dot{s} + F(s)U(s) + \mu^2(1 - e^2) = 0 \quad (11)$$

where  $a$  and  $e$  represent the semi-major axis length and eccentricity, respectively, of a hypothesized SO orbit. The Earth gravitational constant  $\mu = 3.986004418 \times 10^5 \text{ [}\frac{\text{km}^3}{\text{s}^2}\text{]}$  and  $w_1$ ,  $F(s)$ ,  $U(s)$  and  $\gamma_1$  to  $\gamma_4$  are given in [12, appendix A]. Note that these constraints are functions with variables  $s$  and  $\dot{s}$ , and form a 2D nonlinear system of equations. The

solutions of the equations are given in [12, appendix A] with their derivations given in [20, 8, 9]. The PAR procedure was presented in [12], obtaining the birth particle distribution formed as  $\{\gamma^j, \mathbf{x}^j\}_1^{J_B}$ .

The weighted particle distribution  $\{\gamma^j, \mathbf{x}^j\}_1^{J_B}$  is converted into a CGD represented by a mean state  $\bar{\mathbf{x}}$  in the Lie Group  $SE(3) \times \mathbb{R}^3$  and a covariance matrix in the surrounding tangent space using the proposed method in Section 2, and represented by the variables  $\{\bar{\mathbf{x}}, \mathbf{P}\}$ , or equivalently with the notation  $\{\bar{\mathbf{x}}, \mathbf{P}\}$ .

#### 4. THE POISSON LABELED MULTI-BERNOULLI (PLMB) FILTER

This section describes the PLMB filter, which has been used to develop the multi object tracking algorithm. The PLMB filter is capable of modelling any number of new possible targets, and also tracking and identifying targets with a unique label. It is directly applicable to the PUB model, already demonstrated in [9] with the CPHD filter.

The multi-target tracking density is given by a LMB density characterized by its Probability Generating Functional (PGFI)  $G_{\mathcal{X}}^{\text{lmb}}[h]$ , ([7], p. 456), [21]:

$$G_{\mathcal{X}}^{\text{lmb}}[h] = \prod_{\ell \in L} (1 - r_{\ell} + r_{\ell} \langle f_{\ell}(\mathbf{x}), h(\mathbf{x}) \rangle), \quad (12)$$

where, for the RFS  $\mathcal{X}$ ,  $f_{\ell}$  is the single target density of a target with label  $\ell$ ,  $r_{\ell}$  the target's probability of existence and  $h(\mathbf{x})$  a function defined in the space of the individual elements with  $0 \leq h(\mathbf{x}) \leq 1$ .

The birth process is modeled by a Poisson intensity  $D_{\mathcal{B}}(\mathbf{x}) = \lambda_B f_B(\mathbf{x})$ , where  $\lambda_B$  is the expected number of targets to be born with spatial distribution  $f_B(\mathbf{x})$ . The union of Poisson and LMB densities in PGFI form is:

$$G_{\mathcal{X}}^{\text{plmb}}[h] = G_{\mathcal{B}}^{\text{p}}[h] G_{\mathcal{Y}}^{\text{lmb}}[h], \quad (13)$$

where  $G_{\mathcal{B}}^{\text{p}}[h]$  is a Poisson PGFI:

$$G_{\mathcal{B}}^{\text{p}}[h] = e^{D_{\mathcal{B}}[h-1]} \quad (14)$$

and  $G_{\mathcal{Y}}^{\text{lmb}}[h]$  is an LMB PGFI (Equation (12)). Equations (12)–(14) provide in PGFI form, the general PLMB filter equations. Their implementation will be discussed in the following subsections.

##### 4.1 Multi-Target Prediction

For a prior LMB density with parameters  $(r_{\ell}, f_{\ell})$ , and  $\ell \in L$ , where  $L$  is the set of all target labels, the prediction  $(r'_{\ell}, f'_{\ell})$  of the LMB density is given by

$$r'_{\ell} = r_{\ell} \langle P_S, f_{\ell} \rangle \quad \text{and} \quad f'_{\ell}(\mathbf{x}) = \frac{\langle P_S l_x(\mathbf{x}|\cdot), f_{\ell} \rangle}{\langle P_S, f_{\ell} \rangle}, \quad (15)$$

where  $P_S(\mathbf{x})$  is the probability of survival,  $l_x(\mathbf{x}_k|\mathbf{x}_{k-1})$  is the kinematic model, and in general  $\langle \xi, \eta \rangle = \int \xi(\mathbf{x}) \eta(\mathbf{x}) d\mathbf{x}$  represents the inner product.

##### 4.2 Multi-Target Update

The Bayesian update of the Poisson multi-Bernoulli PGFI (13) is a Labeled Multi-Bernoulli Mixture (LMBM) PGFI, which is approximated by an LMB PGFI. The resulting LMBM PGFI is composed of three components: New targets, detected targets, and misdetected targets [11]:

$$G_{\mathcal{X}^+}^+[h] = \prod_{\ell \in L} (1 - r_{\ell}^+ + r_{\ell}^+ \langle f_{\ell}^+, h \rangle), \quad (16)$$

where  $(r_{\ell}^+, f_{\ell}^+)$  are the probability of existence and the probability density of the updated target identified by the label  $\ell$ , respectively.

The probability of existence  $r_{\ell}^+$  is obtained by solving the assignment problem on the cost matrix  $\mathbf{W}_{n,m}$  by applying Loopy Belief Propagation (LBP) [22]. Other methods used to solve the assignment problem are Murty's algorithm [23], and Gibbs sampling [24]. The cost matrix  $\mathbf{W}_{n,m}$  represents the weights of different combinations of targets  $\ell_n$ ,  $n \in 1 \dots N$ , for a total of  $N$  targets and  $M$  measurements  $\mathbf{z}_m$ ,  $m \in 1 \dots M$ . Misdetected targets are represented by  $m = 0$  and  $n \geq 1$  and new born targets are represented by  $n = 0$  and  $m \geq 1$ .

The parameters representing misdetected targets are given by:

$$\mathbf{W}_{n,0} = 1 - r'_{\ell_n} + r'_{\ell_n} \langle (1 - P_D) f'_{\ell_n}, 1 \rangle, \quad (17)$$

$$r_{n,0}^+ = \frac{r'_{\ell_n} \langle (1 - P_D) f'_{\ell_n}, 1 \rangle}{\mathbf{W}_{n,0}}, \quad f_{n,0}^+(\mathbf{x}) = \frac{(1 - P_D(\mathbf{x})) f'_{\ell_n}(\mathbf{x})}{\langle (1 - P_D) f'_{\ell_n}, 1 \rangle}. \quad (18)$$

The parameters representing detected targets are given by:

$$\mathbf{W}_{n,m} = r'_{\ell_n} \langle P_D l_z(\mathbf{z}_m | \cdot) f'_{\ell_n}, 1 \rangle, \quad (19)$$

$$r_{n,m}^+ = 1, \quad f_{\ell_n,m}^+(\mathbf{x}) = \frac{P_D(\mathbf{x}) l_z(\mathbf{z}_m | \mathbf{x}) f'_{\ell_n}(\mathbf{x})}{\langle P_D l_z(\mathbf{z}_m | \cdot) f'_{\ell_n}, 1 \rangle}, \quad (20)$$

and new target labels, which, in this article, are represented by a triplet of the current time step  $k$ , measurement index  $m$  and sensor index  $o$ , are  $\ell_{N+m} = (k, m, o)$ , and their parameters are given by:

$$\mathbf{W}_{0,m} = D_{\mathcal{K}}(\mathbf{z}_m) + \langle D_{\mathcal{B}} l_z(\mathbf{z}_m | \cdot), 1 \rangle, \quad (21)$$

$$r_{0,m}^+ = \frac{\langle D_{\mathcal{B}} l_z(\mathbf{z}_m | \cdot), 1 \rangle}{\mathbf{W}_{0,m}}, \quad f_{0,m}^+(\mathbf{x}) = \frac{D_{\mathcal{B}}(\mathbf{x}) l_z(\mathbf{z}_m | \mathbf{x}, \ell_{N+m})}{\langle D_{\mathcal{B}} l_z(\mathbf{z}_m | \cdot), 1 \rangle}. \quad (22)$$

The uniform distribution of clutter,  $D_{\mathcal{K}}(\mathbf{z}) \approx \lambda_{\kappa} / V_{\kappa}$ , where  $\lambda_{\kappa}$  is the expected number of clutter measurements and  $V_{\kappa}$  the area formed by the sensor FoV. The density  $f_{0,m}^+(\mathbf{x})$  is obtained as a particle distribution by the PAR methodology described in Section 3.

The PUB intensity in Equation (8) can be expressed by separating the observed and non-observed components:

$$D_{\mathcal{B}}(\mathbf{x}) = \lambda_{\beta} \mathcal{U}(\theta(\mathbf{x})) f(\phi(\mathbf{x})) \quad (23)$$

and, therefore,

$$\begin{aligned} \langle D_{\mathcal{B}}(\mathbf{x}) l_z(\mathbf{z}_m | \mathbf{x}), 1 \rangle &\approx \lambda_{\beta} \left\langle \frac{1}{V_{\kappa}} l_z(\mathbf{z}_m | \theta(\mathbf{x})), 1 \right\rangle \left\langle \sum_{i=1}^{J_{\mathcal{B}}} w_b^{(i)} \mathcal{N}(\phi(\mathbf{x}); \bar{\phi}^{(i)}, \mathbf{P}_{\phi}^{(i)}), 1 \right\rangle \\ &= \lambda_{\beta} \frac{1}{V_{\kappa}} \times 1 = \frac{\lambda_{\beta}}{V_{\kappa}}. \end{aligned} \quad (24)$$

The probability of existence  $r_{0,m}^+$  is given by:

$$r_{0,m}^+ = \frac{\lambda_{\beta}}{\lambda_{\kappa} + \lambda_{\beta}} \quad (25)$$

and the cost value  $\mathbf{W}_{0,m}$  is:

$$\mathbf{W}_{0,m} = \frac{\lambda_{\kappa} + \lambda_{\beta}}{V_{\kappa}}. \quad (26)$$

The LBP algorithm returns the weights  $p_{n,m}$  that each assignment has for each label. Pseudo-code for the LBP algorithm can be found in ([22], p. 20). Then, the posterior for previously existing targets is given by:

$$r_{\ell_n}^+ = \sum_{m=0}^M p_{n,m} r_{n,m}^+, \quad f_{\ell_n}^+(\mathbf{x}) = \sum_{m=0}^M p_{n,m} f_{n,m}^+(\mathbf{x}), \quad (27)$$

and for new targets:

$$r_{\ell_{N+m}}^+ = p_{0,m} r_{0,m}^+, \quad f_{\ell_{N+m}}^+(\mathbf{x}) = f_{0,m}^+(\mathbf{x}). \quad (28)$$

Equations (27) and (28) give the parameters of the posterior multi-target distribution of Equation (16).

## 5. SO KINEMATIC PREDICTION MODEL

The following kinematic model is used in the proposed UKF for predicting the required sigma-points.

The equation of satellite motion is assumed to be [25]:

$$\mathbf{a} = -\frac{\mu_E}{\|\mathbf{p}\|^3}\mathbf{p} + \delta_p(\mathbf{p}, \mathbf{v}) + \mathbf{a}_\varepsilon, \quad (29)$$

where  $\mathbf{a} = \dot{\mathbf{v}}$ ,  $\mathbf{v} = \dot{\mathbf{p}}$ ,  $\delta_p(\mathbf{p}, \mathbf{v})$  represents perturbation forces produced by different sources, and  $\mathbf{a}_\varepsilon$  represents non-modeled forces. The predicted state is then given by:

$$\mathbf{x}_{k|k-1}(t_k) = \begin{bmatrix} \mathbf{p}(t_{k-1}) \\ \mathbf{v}(t_{k-1}) \end{bmatrix} + \int_{t_{k-1}}^{t_k} \begin{bmatrix} \mathbf{v}(t) \\ \mathbf{a}(t) \end{bmatrix} dt, \quad (30)$$

where  $t_k$  is the time at time step  $k$ . Each particle of the state is propagated using the method given in [26], using the Shampine–Gordon<sup>1</sup> integrator [27], which models the following forces:

- Earth central gravitation,
- Earth non-spherical forces, such as geopotential, solid tides, ocean tides,
- solar, and lunar gravitation,
- solar radiation pressure.

Further details on the implementation of the model can be found in [26, 28, 3, 29, 30].

Non-modeled perturbations  $\mathbf{a}_\varepsilon$  can be estimated by [25, 31]:

$$\mathbf{a}_\varepsilon(\mathbf{p}(t_{k-1}), \mathbf{v}(t_{k-1}), t, \boldsymbol{\omega}(t_{k-1})) = f_{\text{ric}}^{\text{eci}(\mathbf{p}(t_{k-1}), \mathbf{v}(t_{k-1}))}((t - t_{k-1})\boldsymbol{\omega}(t_{k-1})), \quad (31)$$

where  $\boldsymbol{\omega}$  is a zero-mean Gaussian noise source on the second component in the object's Radial-Intrack-Crosstrack (RIC) frame, and  $f_{\text{ric}}^{\text{eci}}$  is the mapping that transforms a vector in the object's RIC frame to the reference ECI frame (see [12, appendix B]).

Note that Equation (30) can be written in compact form as  $\mathbf{x}_{k|k-1} = f_x(\mathbf{p}_{k-1}, \mathbf{v}_{k-1}, \boldsymbol{\omega})$ .

### 5.1 Lie based Unscented Kalman Filter Prediction

The proposed UKF is partially based on [13, 14] for Lie groups and manifold based target states, respectively. The process noise covariance matrix is given by  $\mathbf{Q}_k = \boldsymbol{\omega}\boldsymbol{\omega}^T$ . The procedure of the proposed SO-LG-UKF is given in Algorithm 1.

## 6. SO OBSERVATION MODEL

An SO detection in a telescopic image is a streak. In this work, SO detection is modeled in terms of the angles  $[\alpha_1, \beta_1, \alpha_2, \beta_2]$  of the streak limits, with respect to the image center, see Figure 1. The FoV of the telescope is within the range  $\alpha \in [-A/2, A/2]$  with respect to the horizontal axis and  $\beta \in [-B/2, B/2]$  with respect to the vertical axis. The measurement is not instantaneous and occurs during an elapsed time known as the *exposure time*  $\Delta t_{\text{exp}}$ . The measurement can then be expressed as:

$$[\alpha, \beta, \dot{\alpha}, \dot{\beta}]^T = \left[ \alpha_1, \beta_1, \frac{\alpha_2 - \alpha_1}{\Delta t_{\text{exp}}}, \frac{\beta_2 - \beta_1}{\Delta t_{\text{exp}}} \right]^T. \quad (32)$$

<sup>1</sup>The Shampine–Gordon integrator is a multi-step method which uses the information from previous steps, in contrast with the Runge–Kutta method, which discards previously calculated information. Therefore, the Shampine–Gordon integrator is more efficient.

---

**Algorithm 1** Unscented Kalman Filter for Lie group space object propagation.
 

---

- 1: **Input:**  $\bar{\mathbf{x}}_{k-1}, \mathbf{P}_{k-1}, \mathbf{Q}_k, \alpha, \kappa;$  ▷ note that  $[\bar{\mathbf{p}}_{k-1}^T \ 1 \ \bar{\mathbf{v}}_{k-1}^T \ 1]^T = \bar{\mathbf{x}}_{k-1}[0 \ 0 \ 0 \ 1 \ 0 \ 0 \ 0 \ 1]^T$
  - 2: **Output:**  $\bar{\mathbf{x}}_{k|k-1}, \mathbf{P}_{k|k-1}$
  - 3:  $\lambda = \alpha^2(q + \kappa) - q$  ▷ scale parameter,  $q = 12$  is the dimension of the augmented vector
  - 4:  $\gamma^0 = \frac{\lambda}{\lambda + q}$
  - 5:  $\gamma^j = \frac{1/2}{\lambda + q}, j = -q, \dots, -1, 1, \dots, q$  ▷ weights
  - 6:  $\mathbf{P}^{\text{aug}} = \text{diag}(\mathbf{P}_{k-1}, \mathbf{Q}_k)$  ▷ augmented covariance matrix
  - 7:  $\boldsymbol{\zeta}_0 = \mathbf{0}$
  - 8:  $\boldsymbol{\zeta}_j = \text{sign}(j) \text{col} \left( \sqrt{(q + \lambda) \mathbf{P}^{\text{aug}}} \right)_j, j = -q, \dots, -1, 1, \dots, q$
  - 9:  $[\boldsymbol{\xi}_j^T \ \boldsymbol{\omega}_j^T] = \boldsymbol{\zeta}_j^T, j = -q, \dots, q$  ▷ note that  $\boldsymbol{\xi}_j^T = [\boldsymbol{\rho}_j^T \ \boldsymbol{\theta}_j^T \ \mathbf{v}_j^T]^T$
  - 10:  $[\mathbf{p}_j^T, 1]^T = \text{Exp\_SE3} \left( [\boldsymbol{\rho}_j^T \ \boldsymbol{\theta}_j^T]^T \right) [\bar{\mathbf{p}}_{k-1}^T, 1]^T, j = -q, \dots, q$  ▷ position component of the  $j$ th sigma-point
  - 11:  $\mathbf{v}_j = \bar{\mathbf{v}}_{k-1} + \mathbf{v}_j, j = -q, \dots, q$  ▷ velocity component of the  $j$ th sigma-point
  - 12:  $\mathbf{x}_{k|k-1}^j = f_x(\mathbf{p}_j, \mathbf{v}_j, \boldsymbol{\omega}_j), j = -q, \dots, q$  ▷ state propagation of the  $j$ th sigma-point
  - 13:  $\{\bar{\mathbf{x}}_{k|k-1}, \mathbf{P}_{k|k-1}\} = \text{PARTICLESTOCGD}(\{\gamma^j, \mathbf{x}_{k|k-1}^j\}_{j=-q}^q)$  ▷ predicted target state
- 

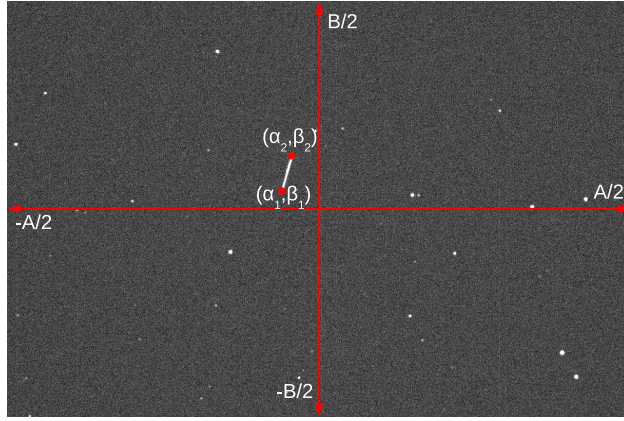


Fig. 1: Image taken from the sidereal tracking of NORAD satellite 25,853, from the Mitre Corporation. Horizontal/vertical arrowed red lines indicate angular axes, red dots indicate the satellite coordinate  $(\alpha_1, \beta_1)$  at  $t_k$  and  $(\alpha_2, \beta_2)$  at  $t_k + \Delta t_{\text{exp}}$ .

An observation model for real image measurements can be found in [32]. The observation model is given by the function  $\hat{\mathbf{z}} = \mathbf{H} f_{\text{eci}}^{\text{cam}}(\mathbf{x})$ , where  $f_{\text{eci}}^{\text{cam}}(\mathbf{x})$  is the projection of the state vector into the camera spherical coordinate system and  $\mathbf{H}$  is the observation matrix:

$$\mathbf{H} = \begin{bmatrix} 0 & 1 & 0 & 0 & 0 & 0 \\ 0 & 0 & 1 & 0 & 0 & 0 \\ 0 & 0 & 0 & 0 & 1 & 0 \\ 0 & 0 & 0 & 0 & 0 & 1 \end{bmatrix}. \quad (33)$$

The single target measurement model is then given by the likelihood function  $l_z(\mathbf{z}|\mathbf{x})$ , modeled by the Gaussian distribution:

$$l_z(\mathbf{z}|\mathbf{x}) = \mathcal{N}(\mathbf{z}; \mathbf{H} f_{\text{eci}}^{\text{cam}}(\mathbf{x}), \mathbf{R}). \quad (34)$$

An observed state  $\hat{\mathbf{z}}_k^j = [\alpha_k^j, \beta_k^j, \dot{\alpha}_k^j, \dot{\beta}_k^j]^T$  can be represented in terms of the telescope image coordinates  $(\alpha_{1,k}^j, \beta_{1,k}^j, \alpha_{2,k}^j, \beta_{2,k}^j) = [\alpha_k^j, \beta_k^j, \alpha_k^j + \Delta t_{\text{exp}} \dot{\alpha}_k^j, \beta_k^j + \Delta t_{\text{exp}} \dot{\beta}_k^j]^T$ .

The single target posterior densities for each target  $\ell$  are calculated based on the procedure in [25]:

1. Sample  $J$  vectors  $\mathbf{x}_j^T = [\mathbf{p}_j^T, \mathbf{x}_j^T]$ ,  $j = 1, \dots, J$ , from the state as follows:

(a) Sample  $\boldsymbol{\xi}^j \sim \mathcal{N}(\mathbf{0}, \mathbf{P}_{k|k-1})$ .

(b) Calculate  $[\mathbf{p}_j^T \ 1 \ \mathbf{v}_j^T \ 1]^T = \text{Exp}(\boldsymbol{\xi}^j)[\bar{\mathbf{p}}_{k-1}^T \ 1 \ \bar{\mathbf{v}}_{k-1}^T \ 1]^T$ .

2. Transform the particles to topocentric camera coordinates:  $\mathbf{y}_j = f_{\text{eci}}^{\text{cam}}(\mathbf{x}_j)$ , with  $\mathbf{y} = [s \ \alpha \ \beta \ s \ \dot{\alpha} \ \dot{\beta}]^T$ .

3. Calculate the probability of detection of each particle as follows:

$$P_D(\mathbf{y}_j) = \begin{cases} P_D, & \text{if } |\alpha_1^j|, |\alpha_2^j| \leq A/2 \ \& \ |\beta_1^j|, |\beta_2^j| \leq B/2 \\ 0, & \text{otherwise,} \end{cases} \quad (35)$$

and the average probability of detection  $\bar{P}_D$ .

4. Calculate weights as  $\gamma_j = P_D(\mathbf{y}_j)/\bar{P}_D$ .

5. Approximate  $\{\gamma_j, \mathbf{y}_j\}_1^J$  as a Gaussian distribution  $(\boldsymbol{\mu}_{k|k-1}, \boldsymbol{\Sigma}_{k|k-1})$ .

6. Update using a linear Kalman filter.

7. Get  $J$  samples  $\mathbf{y}_k^j \sim \mathcal{N}(\boldsymbol{\mu}_k, \boldsymbol{\Sigma}_k)$ . Note that the radial components  $s, \dot{s}$  do not change because they are not observed.

8. Transform from the camera to the ECI frame  $\mathbf{x}_k^j = f_{\text{cam}}^{\text{eci}}(\mathbf{y}_k^j)$ . Thus the updated particle distribution is given by  $\{1/J, \mathbf{x}_k^j\}_1^J$ .

The particle distribution of undetected targets is given by  $\mathbf{x}_k^j = \mathbf{x}_{k|k-1}^j$  with weights:

$$\gamma_k^j = \frac{[1 - P_D(\mathbf{y}_j)]}{1 - \bar{P}_D} \frac{1}{J}. \quad (36)$$

Following the multi-target update procedure of Section 4.2, and also given in [12, Algorithms 2, 3] each updated target has the form  $(\ell, r, \{\gamma_\ell^j, \mathbf{x}_\ell^j\}_1^J)$ , for which the particle distribution is converted to  $\{\tilde{\boldsymbol{\chi}}_k, \mathbf{P}_k\} = \text{PARTICLES TO CGD}(\{\gamma_\ell^j, \mathbf{x}_\ell^j\}_1^J)$ . Finally the updated target distribution is  $(\ell, r, \tilde{\boldsymbol{\chi}}_k, \mathbf{P}_k)$ .

## 7. RESULTS

### 7.1 Target Distance Error Metrics

To quantify the performance of the LG-UKF filter, distance metrics are needed. Since the estimation of SO orbital trajectories is sought in this article, it makes sense to define single SO estimate to ground-truth distance errors in terms of distances along their orbital trajectories, rather than the Euclidean distance between them [12]:

$$d_o(\mathbf{x}_1, \mathbf{x}_2) = \theta_{12} \frac{r_1 + r_2}{2} = \arccos\left(\frac{\mathbf{x}_1}{\|\mathbf{x}_1\|} \cdot \frac{\mathbf{x}_2}{\|\mathbf{x}_2\|}\right) \frac{\|\mathbf{x}_1\| + \|\mathbf{x}_2\|}{2} \quad (37)$$

is the error distance between  $\mathbf{x}_1$  and  $\mathbf{x}_2$ , to be used in the multi-SO error metrics for quantifying the performance of the PLMB filter.

### 7.2 Database Construction

The database is built using simulated telescopic measurements of LEO SOs, obtained from the TLE file of 4 October 2019<sup>2</sup>. The measurements are simulated by projecting the SO trajectories into the image plane of twelve telescopic cameras from the FTN. The name, location, and simulated pointing directions of the telescopes are shown in Table 1.

<sup>2</sup>The TLE file used in the experiments, containing SO trajectory parameters from 2–6 October 2019

Table 1: Location of the observatories of the FTN [15] with their simulated pointing directions.

Telescope (City, State)	Location	Country	Longitude (East)	Latitude	Altitude (Meters)	Azimuth $^\circ$ (Simulated Point- ing Direction)	Elevation $^\circ$ (Simulated Point- ing Direction)
Woodland Park, CO	USA	255.01	39.01	2790	179	5	
Yoder, CO	USA	255.80	38.89	1961	180	5	
Grand Junction, CO	USA	251.76	39.96	1380	176	5	
Durango, CO	USA	252.13	37.27	1880	173	5	
Sterling, CO	USA	256.80	40.65	1177	181	5	
La Junta, CO	USA	256.46	37.97	1221	183	5	
State College, PA	USA	282.17	40.86	317	184	5	
Vicuña	Chile	289.32	-29.99	1139	4	5	
Canberra	Australia	149.17	-35.29	600	260	5	
Gingin	Australia	115.71	-31.36	18	230	40	
Braunschweig	Germany	10.55	52.28	73	69	5	
Cape Town	South Africa	18.46	-33.96	110	103	12	

In the experiment, a subset of ten SOs were used. These SOs are those that produce a higher number of measurements from the telescopes when the sample frequency is one frame every seven seconds.

### 7.3 LG-UKF performance

To compare the performances of both the proposed LG-UKF and particle filter approach of [12], both algorithms were executed thirty times for ten different SOs. The duration of each complete experiment is one day, however, the number of filtering time steps executed is defined as the sum of the number of samples recorded by all of the telescopes, corresponding to passes of each of the ten SOs.

Figure 2 shows an SO's predictions after a time step of almost 2 hours (Figs. 2(a), (b) and (c)) and its update (Fig. 2(d)) at a single time step  $k$ . The meanings of each color and line type in each figure are given in the figure caption. Figures 2(a) and (b) show the predicted state of the SO when the process noise  $\omega$  is high (Fig. 2(a)) and when it is reduced by a factor of five (Fig. 2(b)). The figures demonstrate that the resulting LG-UKF samples (black points) distribute in a "banana" shape according to the  $SE(3) \times \mathbb{R}^3$  space (Equation (1)) as expected. When the process noise  $\omega$  is lower (Fig. 2(b)) the LG-UKF samples and particles (pink points) distribute similarly. Figure 2(c) shows a zoomed view of the LG-UKF sample and particle distributions when  $\omega$  is again reduced by a factor of five. Once again, both distributions are similar. For the same value of  $\omega$ , after update, Fig. 2(d) shows that the estimated distribution of the state  $\chi$  (black points) concentrates around the true SO position, with a significantly reduced covariance.

Figure 3 shows the computational processing time (left) and the displacement error (right) for various targets, with labels  $l = 2, 4$  and  $6$ . As can be seen, the processing time is consistently reduced by an order of magnitude due to the lower number of sigma-points (21) used in the LG-UKF in comparison with the number of particles (200) used in the particle filter.

However, the error is usually higher in the LG-UKF with respect to the particle filter. Usually for very long time step predictions (2 hours), due to the time between telescopic SO observations, the LG-UKF filter loses track of the position (as can be seen in Figure 3(b)).

## 8. CONCLUSIONS

This article has demonstrated that it is possible to significantly reduce the computational processing time required for SO tracking by replacing a particle filter with an LG-UKF which preserves the "banana" shape of the distribution.

A simulated space debris database was created based on TLE data, in which LEO satellites/debris were observed by simulated telescopes based on the FTN. A satellite measurement that corresponds to both ends of detected streaks was converted into celestial coordinates. These coordinate pairs were then used as inputs to the LG-UKF SO tracking algorithm. The experiment simulated measurements observed by twelve telescopes.

A ten-fold computational saving time was demonstrated, although some simulations yielded degradation in state estimation accuracy. Improvements could be possible by using a Lie group based update, which is currently under investigation.

The single target SO tracking concepts in this article are currently being incorporated into the PLMB multi-target tracking framework.

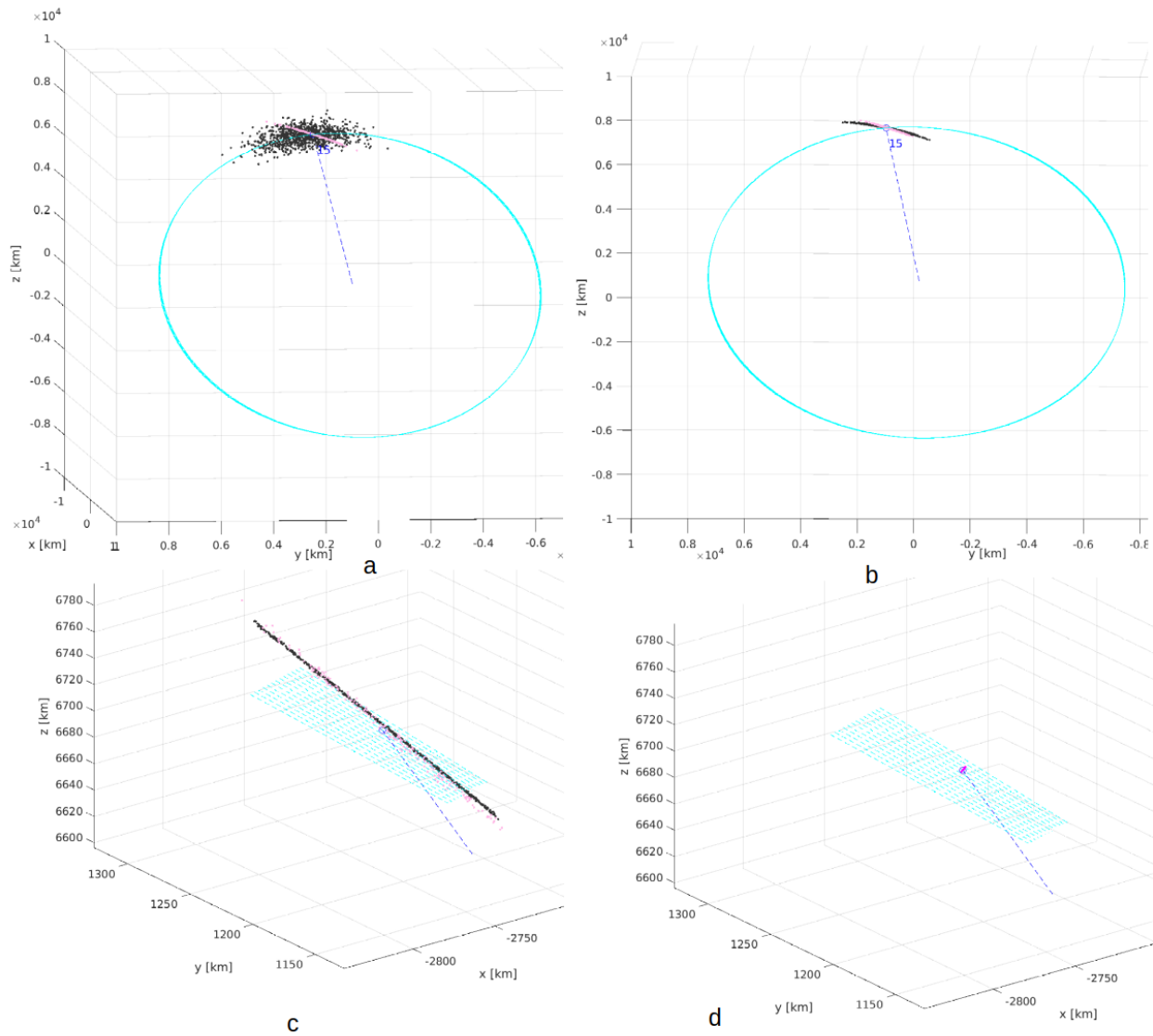
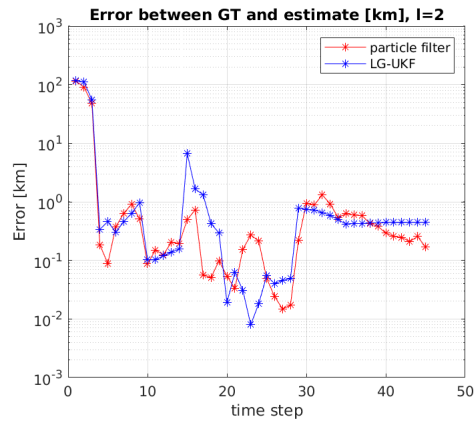
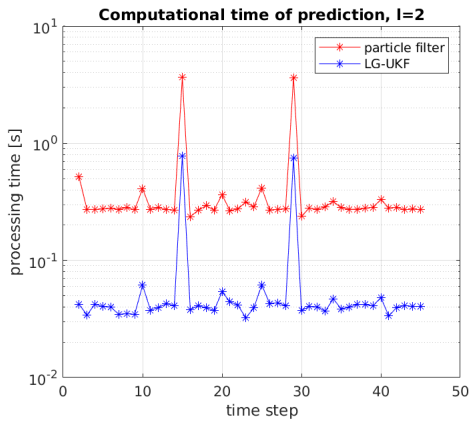
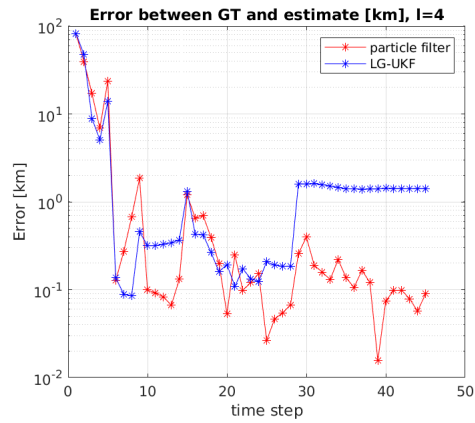
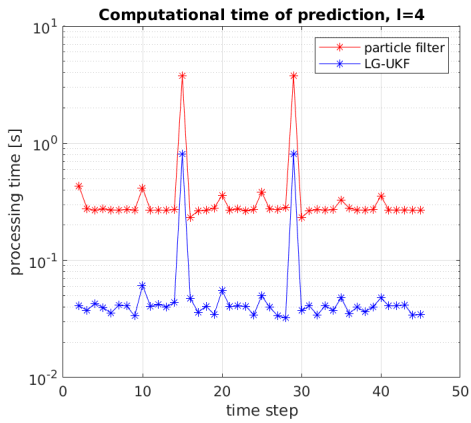


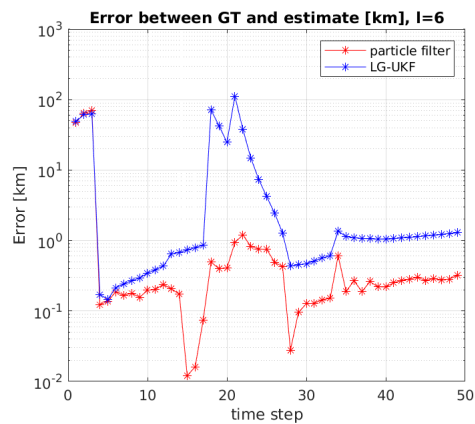
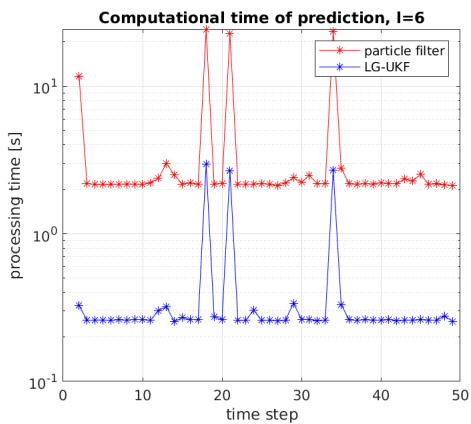
Fig. 2: Experimental SO tracking results under differing process noise levels. The multiple cyan dashed lines correspond to the ground truth trajectory of the SO during multiple passes. Pink points correspond to the particle distribution and black points correspond to LG-UKF distribution. The blue dashed line is a line connecting the center of the Earth and the ground truth SO location.



a



b



c

Fig. 3: Computational processing time (left) and the estimation displacement error (right) for different targets.

## ACKNOWLEDGMENTS

This work was partially sponsored by the U.S. Air Force Office of Scientific Research, Air Force Material Command, under Grant No. FA9550-18-C-0201. It was also partially funded by CONICYT/PIA Project AFB180004, CONICYT FONDECYT Postdoctorado 2018 number 3180319, CONICYT FONDECYT project 1190979 and Becas CONICYT Doctorado Nacional, 2012.

# Appendices

## A. LOGARITHMIC AND EXPONENTIAL MAPS IN MANIFOLDS

### A.1 Mapping in the Unit Sphere $S^2$

Let  $\mathbf{x} \in \mathbb{R}^3$ ,  $\|\mathbf{x}\| = 1$  a vector in the unit sphere.

The logarithmic map of  $\mathbf{x}$ , with respect to  $\bar{\mathbf{x}}$  is given by [16]:

$$\text{Log}_{S^2_{\bar{\mathbf{x}}}}(\mathbf{x}) = \mathbf{u}\theta, \quad \mathbf{u} = \frac{\mathbf{x} - \bar{\mathbf{x}}\cos(\theta)}{\sin(\theta)}, \quad \theta = \arccos(\bar{\mathbf{x}}^T \mathbf{x}), \quad (38)$$

The exponential map of  $\mathbf{u}$ , with respect to  $\bar{\mathbf{x}}$  is given by as:

$$\text{Exp}_{S^2_{\bar{\mathbf{x}}}}(\boldsymbol{\theta}) = \bar{\mathbf{x}}\cos(\theta) + \mathbf{u}\sin(\theta), \quad \theta = \|\boldsymbol{\theta}\|, \quad \mathbf{u} = \frac{\boldsymbol{\theta}}{\theta}. \quad (39)$$

Note that  $\theta$  is the angle between  $\mathbf{x}$  and  $\bar{\mathbf{x}}$ , and  $\boldsymbol{\theta}$  is the unit vector of the tangent space value given by the logarithm function.

### A.2 Mapping in the Lie Group $SO(3)$

The definitions and equations given in  $SO(3)$  and  $SE(3)$  were obtained from [33].

The rotation matrix  $\mathbf{R} \in SO(3)$ , has a Lie Algebra  $\boldsymbol{\theta}^\wedge \in \mathfrak{so}(3)$  representation and the vector  $\boldsymbol{\theta} \in \mathbb{R}^3$ .

The *hat* operator  $\wedge$  in  $SO(3)$  is defined as:

$$\boldsymbol{\theta} = \begin{bmatrix} \theta_x \\ \theta_y \\ \theta_z \end{bmatrix}, \quad \boldsymbol{\theta}^\wedge = \begin{bmatrix} 0 & -\theta_z & \theta_y \\ \theta_z & 0 & -\theta_x \\ -\theta_y & \theta_x & 0 \end{bmatrix}, \quad (40)$$

The *vee* operator  $\vee$  is the inverse of the *hat* operator:

$$(\boldsymbol{\theta}^\wedge)^\vee = \begin{bmatrix} 0 & -\theta_z & \theta_y \\ \theta_z & 0 & -\theta_x \\ -\theta_y & \theta_x & 0 \end{bmatrix}^\vee = \begin{bmatrix} \theta_x \\ \theta_y \\ \theta_z \end{bmatrix} \quad (41)$$

The logarithmic map is given by:

$$\text{Log}_{SO3}(\mathbf{R}) = \frac{\boldsymbol{\theta}(\mathbf{R} - \mathbf{R}^T)^\vee}{2 \sin \theta}, \quad \theta = \arccos\left(\frac{\text{trace}(\mathbf{R}) - 1}{2}\right) \quad (42)$$

The exponential map is given by:

$$\text{Exp}_{SO3}(\boldsymbol{\theta}) = \mathbf{I} + \sin \theta \boldsymbol{\theta}^\wedge + (1 - \cos \theta) \boldsymbol{\theta}^\wedge^2, \quad \theta = \|\boldsymbol{\theta}\|, \quad \mathbf{u} = \boldsymbol{\theta}/\theta \quad (43)$$

### A.3 Mapping in the Lie Group $SE(3)$

An element  $\mathbf{H} \in SE(3)$  is written as:

$$\mathbf{H} = \begin{bmatrix} \mathbf{R} & \mathbf{t} \\ \mathbf{0} & 1 \end{bmatrix} \quad (44)$$

where  $\mathbf{R} \in SO(3)$  is a rotation matrix and  $\mathbf{t} \in \mathbb{R}^3$  is a translation vector. The vector tangent and Lie Algebra are given by:

$$\boldsymbol{\tau} = \begin{bmatrix} \boldsymbol{\rho} \\ \boldsymbol{\theta} \end{bmatrix} \in \mathbb{R}^6, \quad \boldsymbol{\tau}^\wedge = \begin{bmatrix} \boldsymbol{\theta}^\wedge & \boldsymbol{\rho} \\ \mathbf{0} & 0 \end{bmatrix} \in \mathfrak{se}(3). \quad (45)$$

The exponential map is given by:

$$\text{Exp\_SE3}(\boldsymbol{\tau}) = \begin{bmatrix} \text{Exp\_SO3}(\boldsymbol{\tau}) & \mathbf{V}\boldsymbol{\rho} \\ \mathbf{0} & 1 \end{bmatrix}, \quad \mathbf{V} = \mathbf{I} + \frac{1 - \cos \theta}{\theta^2} \boldsymbol{\theta}^\wedge + \frac{\theta - \sin \theta}{\theta^3} \boldsymbol{\theta}^{\wedge 2} \quad (46)$$

The logarithmic map is given by:

$$\text{Log\_SE3}(\mathbf{H}) = \begin{bmatrix} \mathbf{V}^{-1}\mathbf{t} \\ \boldsymbol{\theta} \end{bmatrix}, \quad \boldsymbol{\theta} = \text{Log\_SO3}(\mathbf{R}), \quad \mathbf{V}^{-1} = \mathbf{I} - \frac{\boldsymbol{\theta}^\wedge}{2} + \left(1 - \frac{\theta}{2} \frac{\sin \theta}{1 - \cos \theta}\right) \left(\frac{\boldsymbol{\theta}^\wedge}{\theta}\right)^2 \quad (47)$$

### A.4 Mapping in the Lie Group $SE(3) \times \mathbb{R}^3$

An element  $\mathbf{A} \in SE(3) \times \mathbb{R}^3$  is written as:

$$\mathbf{A} = \begin{bmatrix} \mathbf{H} & \mathbf{0} \\ \mathbf{0} & \mathbf{B} \end{bmatrix}, \quad \text{with } \mathbf{B} = \begin{bmatrix} \mathbf{I} & \mathbf{b} \\ \mathbf{0} & 1 \end{bmatrix} \quad (48)$$

where  $\mathbf{H} \in SE(3)$  and  $\mathbf{B}$  is the representation of  $\mathbf{b} \in \mathbb{R}^3$ . The vector tangent is given by  $\boldsymbol{\tau} = [\boldsymbol{\rho}^T \boldsymbol{\theta}^T \mathbf{b}^T]^T$ .

The exponential map is given by:

$$\text{Exp}(\boldsymbol{\tau}) = \begin{bmatrix} \text{Exp\_SE3}([\boldsymbol{\rho}^T \boldsymbol{\theta}^T]^T) & \mathbf{0} \\ \mathbf{0} & \mathbf{B} \end{bmatrix}. \quad (49)$$

The logarithmic map is given by:

$$\text{Log}(\mathbf{A}) = \begin{bmatrix} \text{Log\_SE3}(\mathbf{H}) \\ \mathbf{b} \end{bmatrix}. \quad (50)$$

## REFERENCES

- [1] Andrea Milani, Giovanni F Gronchi, Mattia De Michieli Vitturi, and Zoran Knežević. Orbit determination with very short arcs. I admissible regions. In *Celestial Mechanics and Dynamical Astronomy*, pages 59–87. Universita di Pisa, Pisa, Italy, dec 2004.
- [2] Kyle J DeMars and Moriba K Jah. Probabilistic initial orbit determination using gaussian mixture models. *Journal of Guidance, Control, and Dynamics*, 36(5):1324–1335, 2013.
- [3] Emmanuel D Delande, C Frueh, Jeremie Houssineau, and Daniel E Clark. Multi-object filtering for space situational awareness. In *AAS Space Flight Mechanics Meeting*, 2015.
- [4] Yaakov Bar-Shalom and Xiao-Rong Li. *Multitarget-multisensor tracking: principles and techniques*, volume 19. YBs Storrs, CT, 1995.
- [5] Samuel S Blackman. Multiple hypothesis tracking for multiple target tracking. *IEEE Aerospace and Electronic Systems Magazine*, 19(1):5–18, 2004.
- [6] Ronald P S Mahler. *Statistical Multisource-multitarget Information Fusion*. Artech House Publishers, jan 2007.
- [7] R.P.S. Mahler. *Advances in Statistical Multisource-Multitarget Information Fusion*. Artech House, Norwood, MA, USA, 2014.
- [8] I Hussein, C Roscoe, M Wilkins, and P Schumacher. Probabilistic Admissible Region for Short-Arc Angles-Only Observations. In *Proceedings of the Advanced Maui Optical and Space Surveillance Technologies Conference*, sep 2014.

- [9] Brandon A Jones. CPHD filter birth modeling using the probabilistic admissible region. *IEEE Transactions on Aerospace and Electronic Systems*, 54(3):1456–1469, 2018.
- [10] S Reuter, Ba-Tuong Vo, Ba-Ngu Vo, and K Dietmayer. The Labeled Multi-Bernoulli Filter. *IEEE Transactions on Signal Processing*, 62(12):3246–3260, June 2014.
- [11] Leonardo Cament, Javier Correa, Martin Adams, and Claudio Pérez. The histogram poisson, labeled multi-Bernoulli multi-target tracking filter. *Signal Processing*, page 107714, 2020.
- [12] Leonardo Cament, Martin Adams, and Pablo Barrios. Space debris tracking with the poisson labeled multi-bernoulli filter. *Sensors*, 21(11):3684, 2021.
- [13] Martin Brossard, Silvere Bonnabel, and Jean-Philippe Condomines. Unscented kalman filtering on lie groups. In *2017 IEEE/RSJ International Conference on Intelligent Robots and Systems (IROS)*, pages 2485–2491. IEEE, 2017.
- [14] Martin Brossard, Axel Barrau, and Silvere Bonnabel. A code for unscented kalman filtering on manifolds (ukf-m). In *2020 IEEE International Conference on Robotics and Automation (ICRA)*, pages 5701–5708. IEEE, 2020.
- [15] Francis K Chun and et al. A new global array of optical telescopes: The Falcon telescope network. *Publications of the Astronomical Society of the Pacific*, 130(991):095003–, sep 2018.
- [16] Sylvain Calinon and Noémie Jaquier. Gaussians on riemannian manifolds for robot learning and adaptive control. *arXiv preprint arXiv:1909.05946*, 2019.
- [17] Ángel F García-Fernández, Jason L Williams, Karl Granstrom, and Lennart Svensson. Poisson multi-Bernoulli mixture filter: direct derivation and implementation. *IEEE Transactions on Aerospace and Electronic Systems*, 54(4):1883–1901, August 2018.
- [18] Ba-Ngu Vo and Ba-Tuong Vo. An implementation of the multi-sensor generalized labeled multi-bernoulli filter via gibbs sampling. In *2017 20th International Conference on Information Fusion (Fusion)*, pages 1–8. IEEE, 2017.
- [19] Islam I Hussein, Christopher WT Roscoe, Matthew P Wilkins, and Paul W Schumacher Jr. Probabilistic admissibility in angles-only initial orbit determination. In *Proceedings of the 24th International Symposium on Space Flight Dynamics*, pages 5–9, 2014.
- [20] Jose Franco, Emmanuel D Delande, Carolin Frueh, Jeremie Houssineau, and Daniel E Clark. A spherical co-ordinate space parameterisation for orbit estimation. In *2016 IEEE Aerospace Conference*, pages 1–12. IEEE, 2016.
- [21] Ronald Mahler. On CPHD filters with track labeling. In *Signal Processing, Sensor/Information Fusion, and Target Recognition XXVI*, volume 10200, page 102000E. International Society for Optics and Photonics, 2017.
- [22] Jason L Williams. Marginal multi-bernoulli filters - RFS derivation of MHT, JIPDA, and association-based member. *IEEE Trans. Aerospace and Electronic Systems*, 51(3):1664–1687, 2015.
- [23] Katta G Murthy. An algorithm for ranking all the assignments in order of increasing costs. *Operations research*, 16(3):682–687, 1968.
- [24] Stephan Reuter, Andreas Danzer, Manuel Stuebler, Alexander Scheel, and Karl Granström. A fast implementation of the Labeled Multi-Bernoulli filter using gibbs sampling. *Intelligent Vehicles Symposium*, pages 765–772, 2017.
- [25] E Delande, Jeremie Houssineau, Jose Franco, C Frueh, D Clark, and M Jah. A new multi-target tracking algorithm for a large number of orbiting objects. *Advances in Space Research*, 64(3):645–667, 2019.
- [26] Meysam Mahooti and Mohammad Sharifi. Variable and fixed step integrations for dynamic orbit determination of leo satellites. In *The 9th Conference of Iranian Aerospace Society*, 02 2009.
- [27] Matthew M Berry. *A variable-step double-integration multi-step integrator*. PhD thesis, Virginia Tech, 2004.
- [28] Mahendra Mallick, Steve Rubin, and Ba-Ngu Vo. An introduction to force and measurement modeling for space object tracking. In *Proceedings of the 16th International Conference on Information Fusion*, pages 1013–1020. IEEE, 2013.
- [29] G Beutler, T Schildknecht, U Hugentobler, and W Gurtner. Orbit determination in satellite geodesy. *Advances in Space Research*, 31(8):1853–1868, 2003.
- [30] Thomas D Papanikolaou and Dimitrios Tsoulis. Assessment of numerical integration methods in the context of low earth orbits and inter-satellite observation analysis. *Acta Geodaetica et Geophysica*, 51(4):619–641, 2016.
- [31] Emmanuel Delande, Jérémie Houssineau, and Moriba Jah. Physics and human-based information fusion for improved resident space object tracking. *Advances in Space Research*, 62(7):1800–1812, 2018.
- [32] James S McCabe, Kyle J DeMars, and Carolin Frueh. Integrated detection and tracking for multiple space objects. In *AAS Space Flight Mechanics Meeting*, 2015.
- [33] Joan Solà Ortega, Jérémie Deray, and Dinseh Atchuthan. A micro lie theory for state estimation in robotics. 2018.